



Figures and figure supplements

Dynamics of the IFT machinery at the ciliary tip

Alexander Chien *et al*

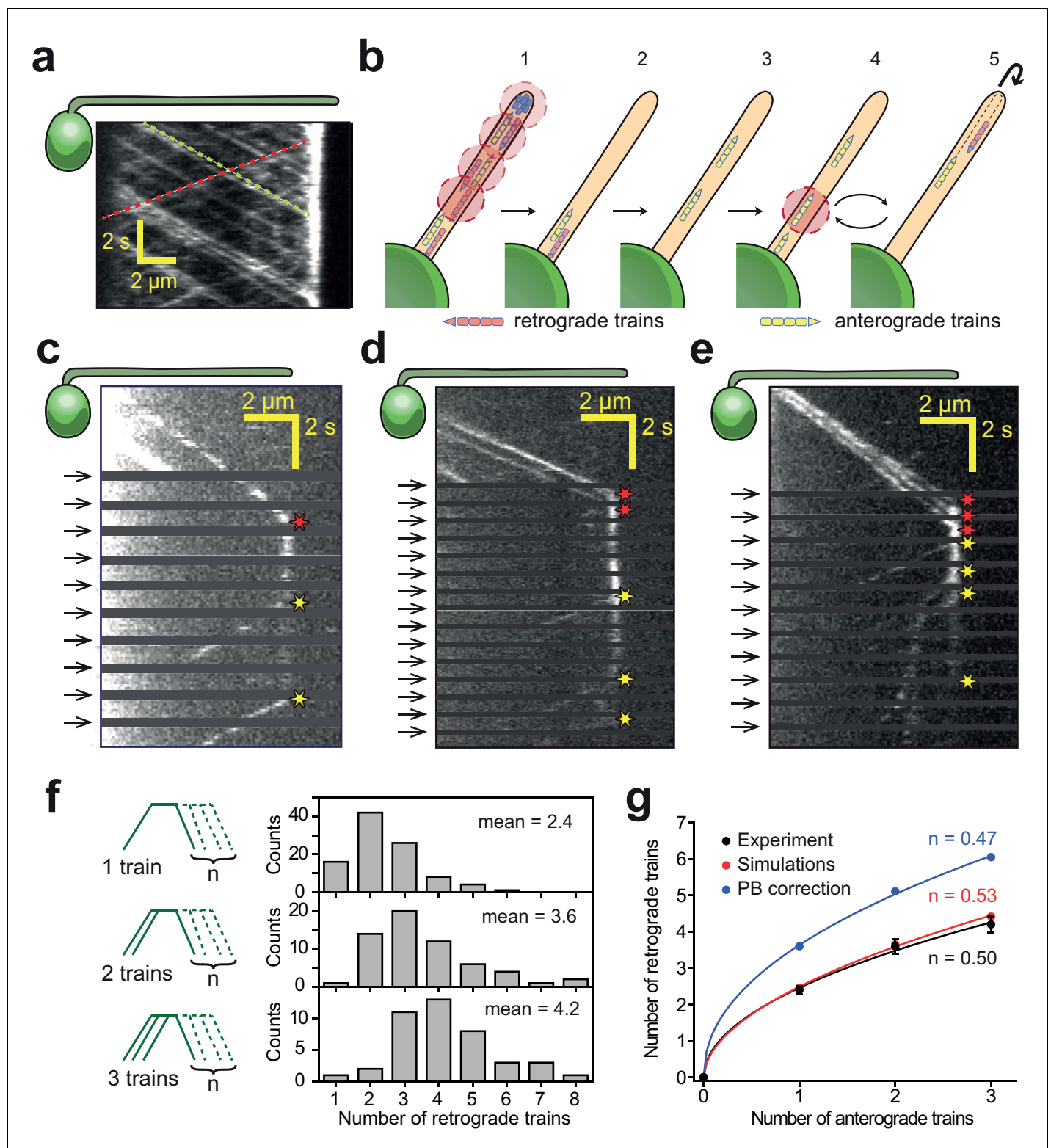


Figure 1. IFT trains split apart and mix with each other at the flagellar tip. (a) Kymograph of a surface-immobilized *pf18* IFT27-GFP strain shows that IFT trains move bidirectionally along the flagellum, only reversing direction at the tip and the base. Multiple IFT trains accumulate at the flagellar tip. Representative anterograde and retrograde trajectories are shown with yellow and red dashed lines, respectively. (b) Schematic representation of the PhotoGate assay. (1) The distal half of the flagellum is prebleached by moving the powerful gate beam from the flagellar tip to near the base of the flagellum. (2–3) The gate beam is turned off to allow a single anterograde train to enter the flagellum without photobleaching. (4) The beam is then

Figure 1 continued on next page

Figure 1 continued

repeatedly turned on for 0.2 s to photobleach the successive trains entering the flagellum and (5) turned off for 0.8 s to image the single fluorescent train within the flagellum. Photobleached trains are not shown. (c–e) Kymographs of one (c), two (d) and three (e) fluorescent anterograde trains entering the flagellum. Anterograde trains pause at the flagellar tip and split into multiple retrograde trains that move back to the base. Arrival of fluorescent anterograde trains and departure of retrograde trains at the tip are shown with red and yellow stars, respectively. Arrows represent repetitive bleaching events near the base of the flagellum. (f) (Left) The number of fluorescent retrograde trains was quantified as a function of one, two or three fluorescent anterograde trains entering the flagellum after photobleaching. (Right) The average number of retrograde trains increased sub-proportionally with the number of fluorescent anterograde trains entering the flagellum. $N = 97, 60, 42$ train events from top to bottom, in 160 cells, from 13 independent experiments. (g) The number of detectable retrograde trains versus the numbers of incoming anterograde trains in PhotoGate experiments and Monte Carlo simulations (PB: photobleaching). Solid lines represent the fit of data to the power law ($y = ax^n$). n is less than one under each condition. Error bars represent s.e.m. ($N = 10,000$ for simulations).

DOI: <https://doi.org/10.7554/eLife.28606.003>

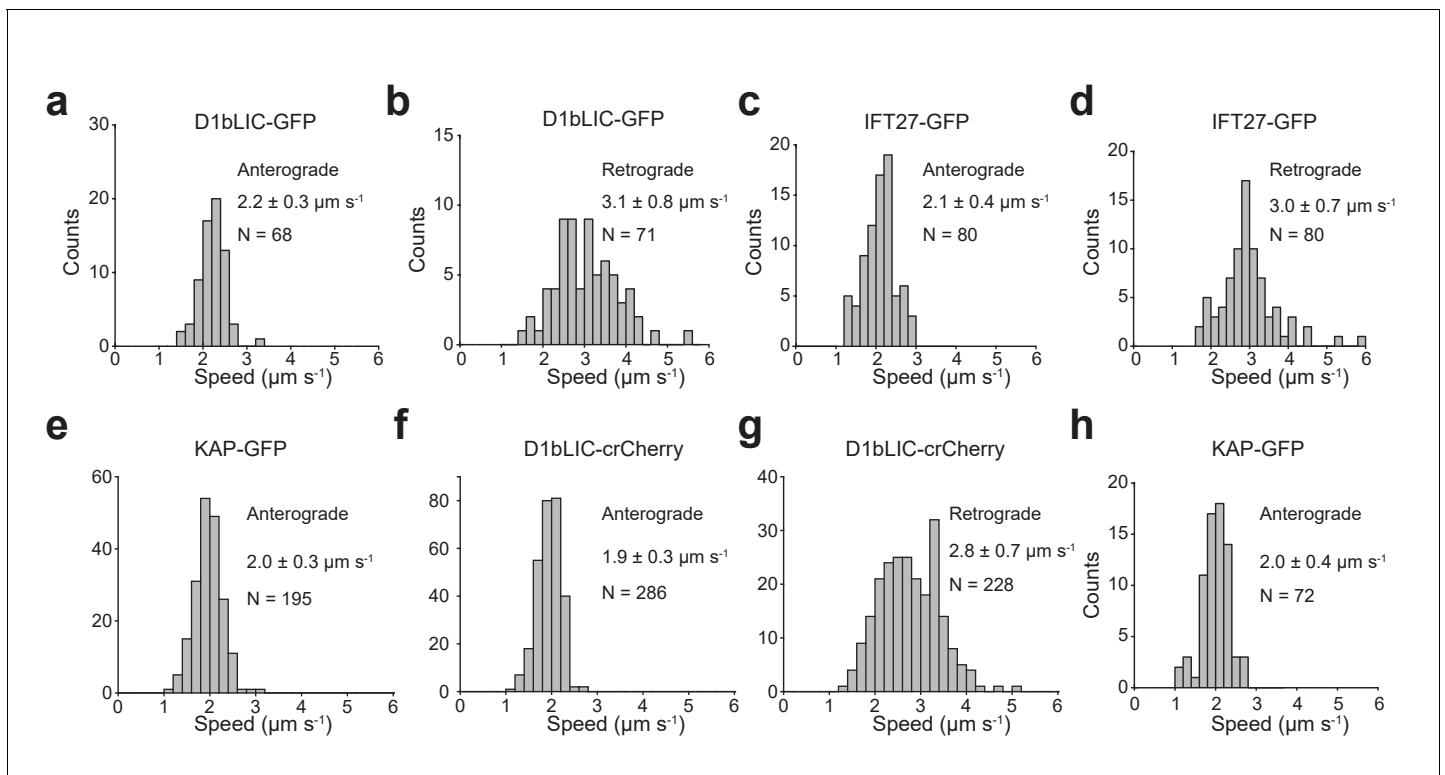


Figure 1—figure supplement 1. Anterograde and retrograde velocities of epitope-tagged IFT27, KAP, and D1bLIC. (a,b) Anterograde (a) and retrograde (b) velocities of D1bLIC-GFP in *d1blic::D1bLIC-GFP* cells. (c, d) Anterograde (c) and retrograde (d) velocities of IFT27-GFP in *pf18 IFT-27-GFP* cells. (e) Anterograde velocities of KAP-GFP in *d1blic::D1bLIC-crCherry KAP-GFP* cells. (f, g) Anterograde (f) and retrograde (g) velocities of D1bLIC-crCherry in *d1blic::D1bLIC-crCherry KAP-GFP* cells. (h) Anterograde velocities of KAP-GFP in *fla3::KAP-GFP* cells. All velocities are reported as mean \pm s.d. N represents the number of trains measured.

DOI: <https://doi.org/10.7554/eLife.28606.004>

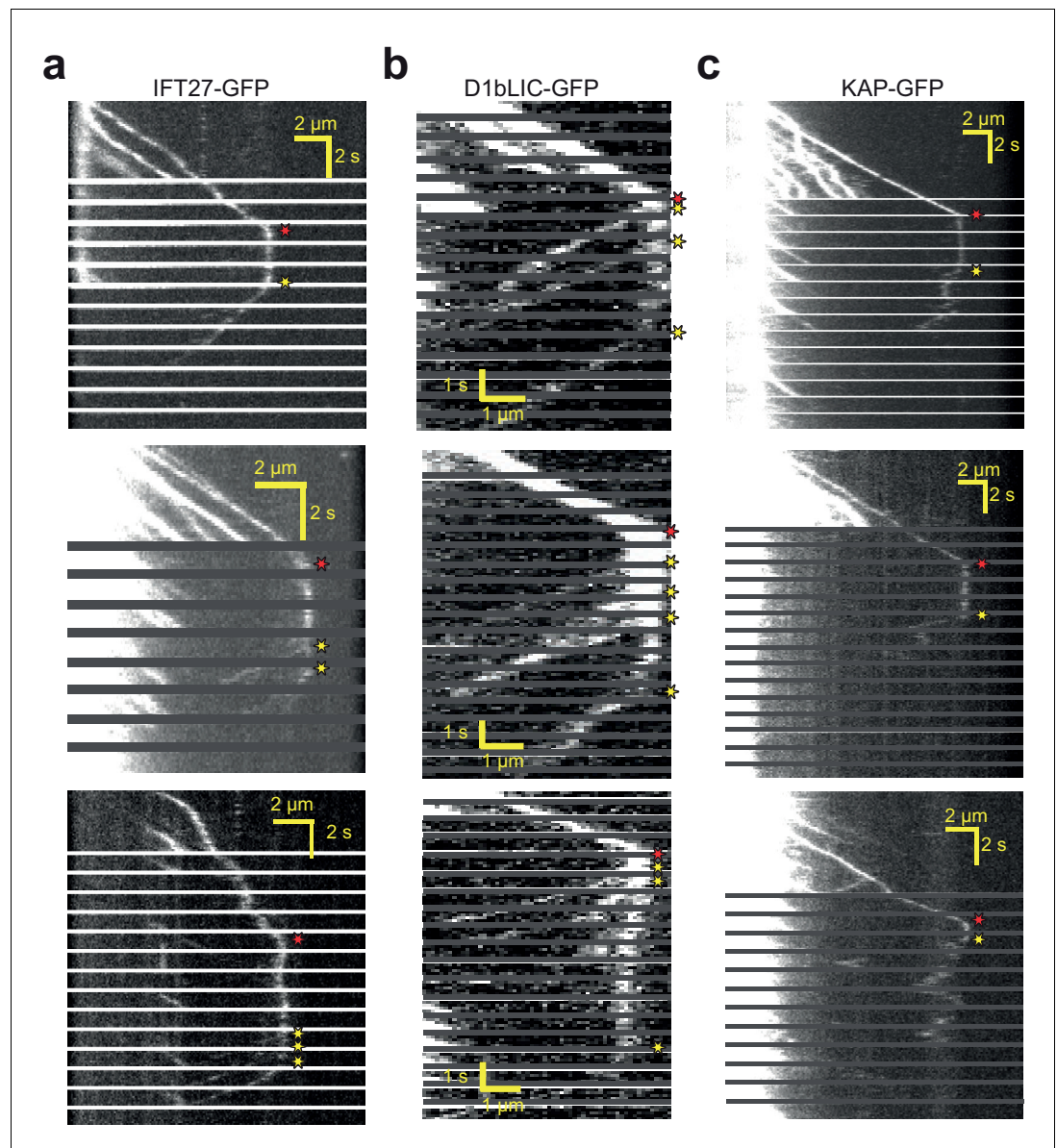


Figure 1—figure supplement 2. Additional examples for PhotoGate imaging of IFT27, D1bLIC, and KAP. (a) IFT27 is moved to the tip on anterograde trains, remodels at the tip, and is returned to the flagellar base on retrograde trains. (b) Dynein is moved to the tip on anterograde trains, remodels at the tip, and moves retrogradely to the cell body. (c) Kinesin moves anterograde trains to the flagellar tip, dissociates from the IFT trains at the tip, and diffuses within the flagellum. Red and yellow stars indicate arrival to and departure from the tip, respectively.

DOI: <https://doi.org/10.7554/eLife.28606.005>

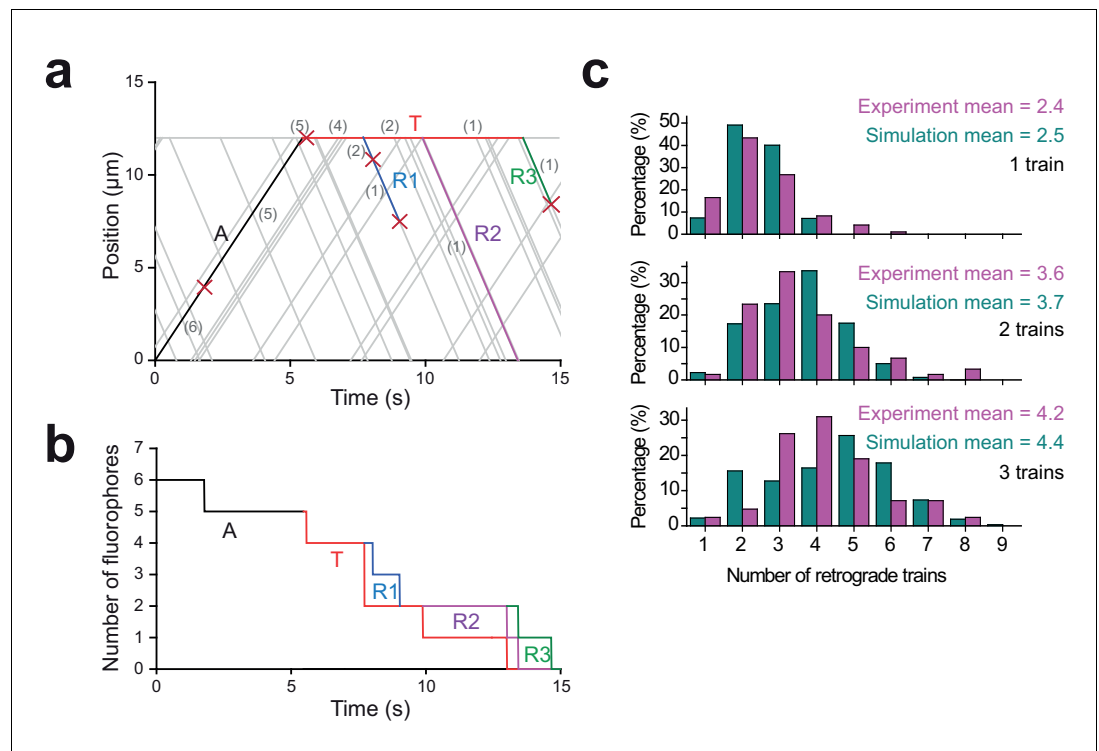


Figure 1—figure supplement 3. Monte Carlo simulations for the dynamics of IFT trains at the flagellar tip. (a) A simulated kymograph with one anterograde IFT train (label A, black line) reaching the flagellar tip, joining the pool at the tip (label T, red line), and returning as three retrograde IFT trains (label R1-R3; blue, purple, and green lines). The anterograde train originally carries six bright fluorophores, and each fluorophore either bleaches or returns back to the flagellar base. The number of fluorophores is labeled in grey within parentheses, and each bleaching event is indicated by a red cross. (b) The total number of fluorophores in the anterograde train (label A, black line), at the flagellar tip (label T, red line), and the retrograde trains (label R1-R3, blue line, purple line and green line) are shown as a function of time for the example kymograph shown in (a). Step-by-step reduction in GFP numbers in anterograde and retrograde trains is due to photobleaching of GFPs at 0.07 s^{-1} under TIR illumination. (c) The number of detectable retrograde trains in PhotoGate assays with one, two, and three fluorescent anterograde trains arriving at the tip in experiments (**Figure 1f**) and Monte Carlo simulations ($N = 10,000$ for simulations).

DOI: <https://doi.org/10.7554/eLife.28606.006>

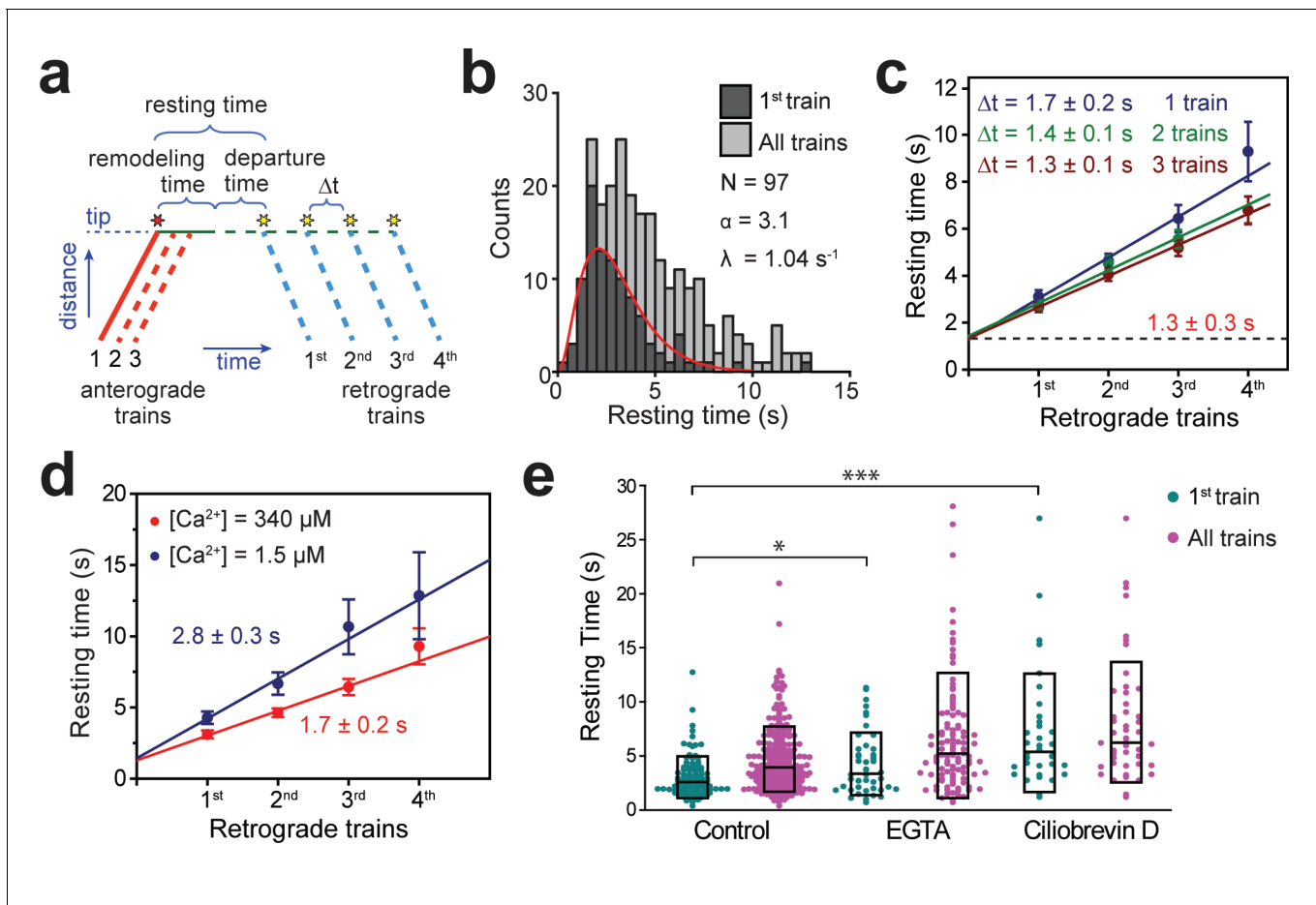


Figure 2. Tip turnaround of IFT trains is a multistep process regulated by dynein activity and extracellular Ca^{2+} . (a) The schematic describes the definition of tip resting time, remodeling time, and departure time measured from the kymographs. Arrival of the first fluorescent anterograde train and the departure of retrograde trains are shown with red and yellow stars, respectively. Tip resting time and departure time are only shown for the first retrograde train. Tip remodeling time is assumed to be the same for each train. Δt represents the time between the departure of successive retrograde trains. (b) The tip resting time histogram of the first retrograde IFT27-GFP train (dark grey) and all of the trains (light grey) emanating from a single anterograde train. The histogram of the first retrograde trains was fitted to a Gamma function (red curve). α and λ are shape and rate parameters, respectively. (c) The linear fit to the average tip resting time reveals Δt between successive trains. The y-intercept (black dashed line) represents the tip remodeling time. Errors represent standard error of the linear fit. (d) Average tip resting times of the first, second, third, and fourth retrograde IFT27-GFP trains coming out of an anterograde train for cells in TAP media (red, $N = 97$) and calcium-depleted media (blue, $N = 44$). Errors represent standard error of the linear fit. (e) IFT27-GFP tip resting times in 0.5 mM EGTA and 0.1 mM ciliobrevin D treated cells. The line within the boxplot represents the mean. The outer edges of the box represent standard deviation. $N = 97, 241, 44, 109, 34$, and 48 retrograde trains from left to right, in a total of 20 independent experiments (Welch's t-test, * $p < 0.05$, *** $p < 0.001$, as compared to no treatment for first retrograde trains).

DOI: <https://doi.org/10.7554/eLife.28606.011>

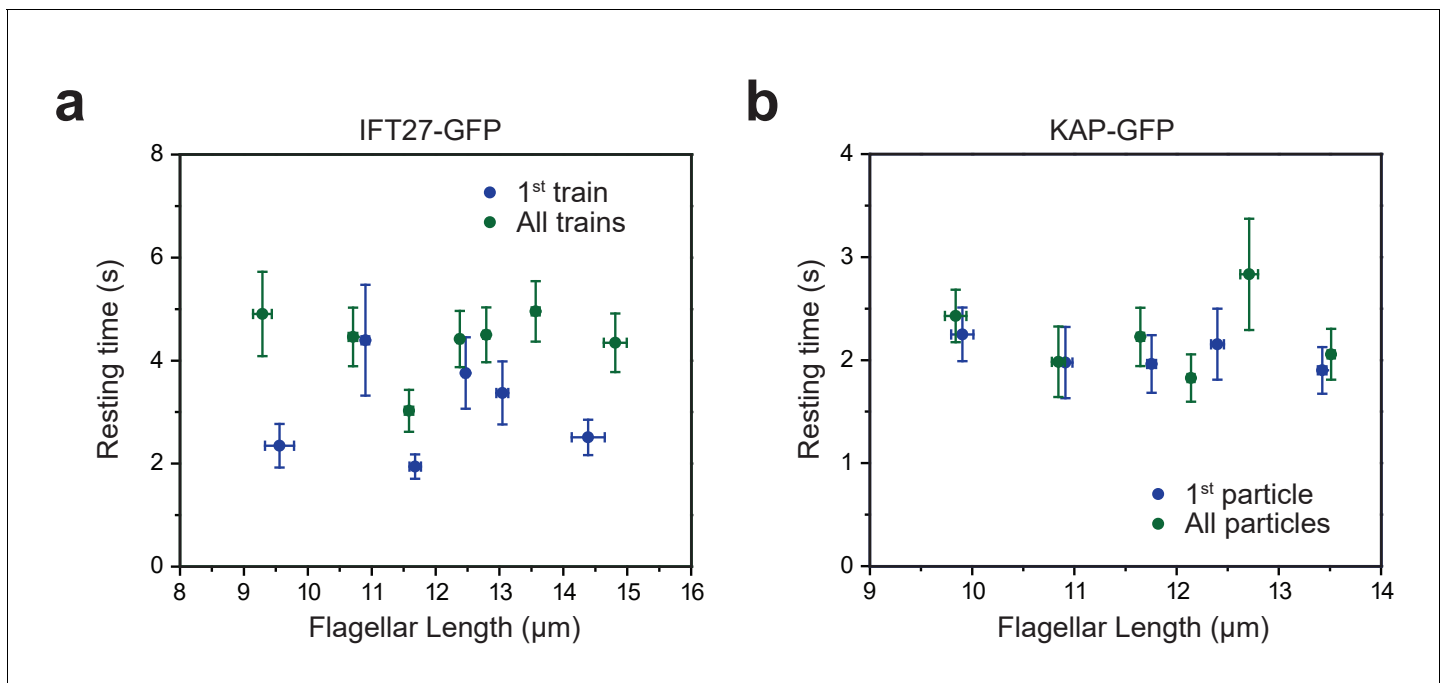


Figure 2—figure supplement 1. Tip resting time is independent of flagellar length. (a,b) The average tip resting time of IFT27-GFP trains (a) and KAP-GFP particles (b) at different lengths of steady-state flagella. Error bars in both axes represent s.e.m. For IFT27-GFP, N = 60 (first train) and 136 (all trains). The bin size is 10 particles. For KAP-GFP, N = 95 (first particle) and 111 (all particles). The bin size is 20 particles.

DOI: <https://doi.org/10.7554/eLife.28606.012>

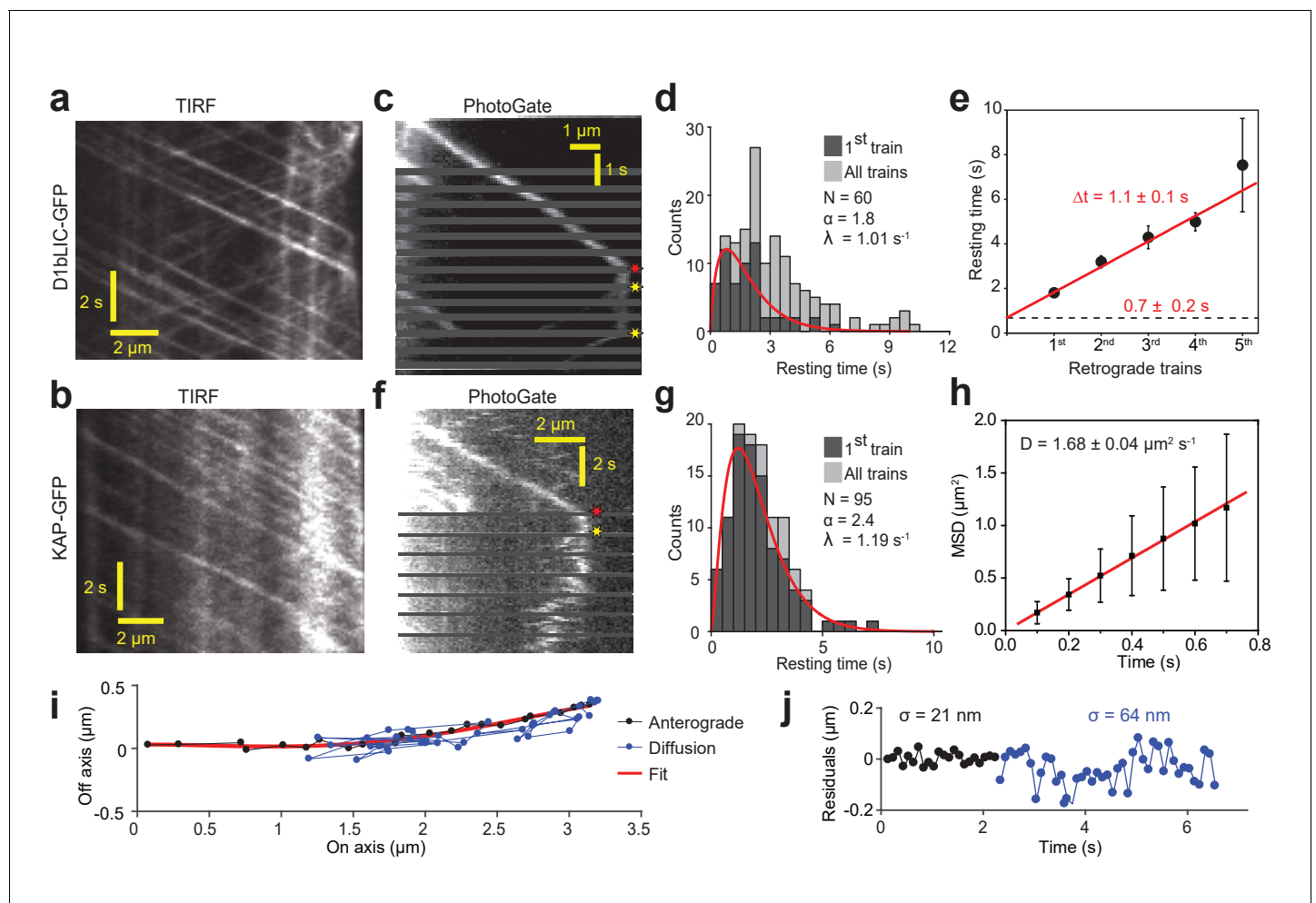


Figure 3. PhotoGate reveals the tip turnaround behavior of IFT motors. (a) In a conventional TIR assay, anterograde and retrograde D1bLIC-GFP traces were clearly visible, but the tip behavior of individual trains could not be discerned. (b) In a conventional TIR assay, KAP-GFP was observed to move anterogradely, but the retrograde transport of KAP was rarely observed. (c) PhotoGate imaging of D1bLIC-GFP shows that D1bLIC trains move to the tip anterogradely, split into multiple trains, and return to the base retrogradely. Red and yellow stars indicate arrival to and departure of D1bLIC-GFP from the tip, respectively. (d) The tip resting time histogram of D1bLIC-GFP. Tip resting time of the first retrograde trains are fit to a Gamma distribution (red curve; 95% c.i. for α is 1.30–2.52 and for λ is 0.69–1.47 s^{-1}). $N = 60$ anterograde trains in 60 cells over nine independent experiments. (e) Averaged tip resting time of the first, second, third, and fourth retrograde D1bLIC-GFP particles returning from the tip (mean \pm s.e.m.). (f) Kymograph analysis of a KAP-GFP cell imaged by PhotoGate. KAP undergoes active transport in the anterograde direction, pauses at the flagellar tip, and diffuses back to the flagellar base. (g) The tip resting time histogram of KAP-GFP. The red curve represents a fit of first train resting times to a Gamma distribution. $N = 95$ anterograde trains in 47 cells over four independent experiments (95% c.i. for α is 1.87–3.19 and for λ is 0.88–1.60 s^{-1}). (h) MSD analysis of KAP-GFP diffusion after it leaves the flagellar tip reveals the average diffusion constant ($N = 27$, mean \pm s.e.m.). (i) High-resolution tracking of a KAP-GFP particle reveals the two-dimensional trajectory during anterograde transport and diffusion. The red curve is the polynomial fit to the trace. (j) The residual plot to the trace in (i) reveals lateral fluctuations (σ) during anterograde transport (black) and diffusion (blue).

DOI: <https://doi.org/10.7554/eLife.28606.013>

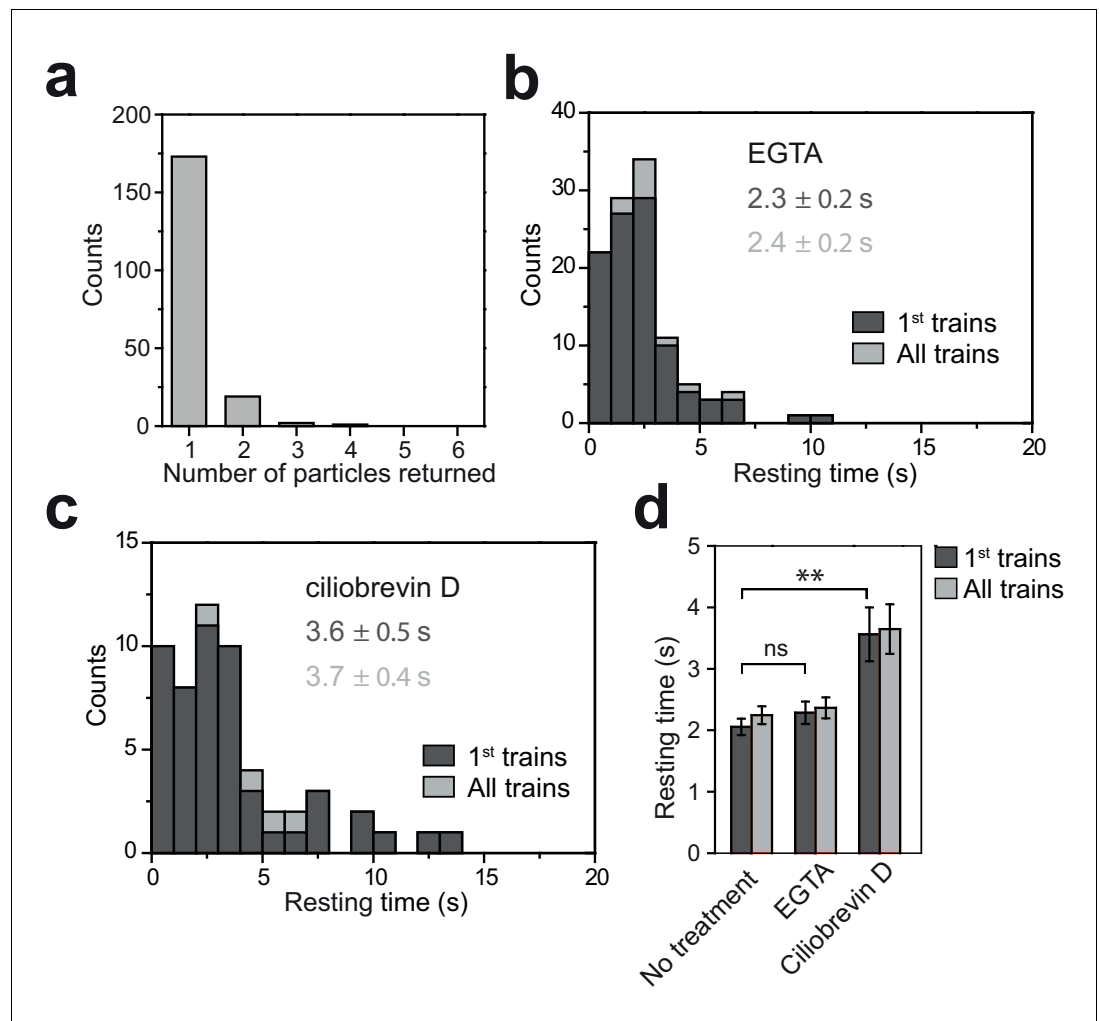


Figure 3—figure supplement 1. Tip resting time of KAP-GFP under EGTA and ciliobrevin D treatments. (a) The number of fluorescent KAP particles emanating from a single fluorescent anterograde KAP particle at the tip. N = 195 trains in 106 cells over nine independent experiments. All KAP clusters displayed diffusive movement after leaving the tip. (b) The tip resting time histogram of KAP-GFP with EGTA treatment. N = 100 trains in 59 cells over five independent experiments. (c) Tip resting time histogram of KAP-GFP with ciliobrevin D treatment. N = 52 trains in 37 cells over four independent experiments (mean \pm s.e.m.). (d) The average tip resting time for KAP-GFP under EGTA and ciliobrevin D treatments (** $p < 0.01$ as compared to no treatment; ns is non-significant). Error bars represent s.e.m.

DOI: <https://doi.org/10.7554/eLife.28606.014>

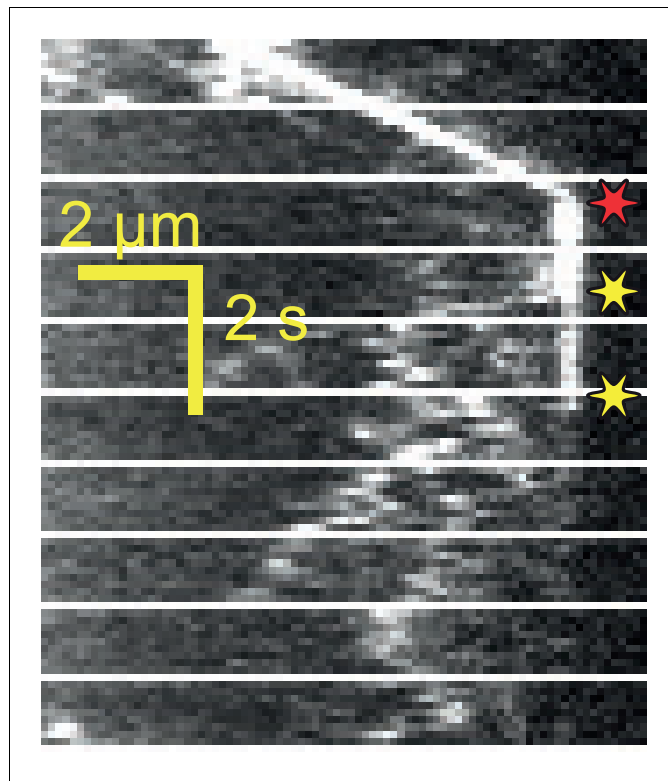


Figure 3—figure supplement 2. Example kymograph of KAP particle breaking apart after tip departure. Kinesin moves anterograde trains to the flagellar tip, dissociates from the IFT trains at the tip, and diffuses within the flagellum. In this example, the KAP particle breaks apart into smaller particles while diffusing. Red and yellow stars indicate arrival to and departure from the tip, respectively.

DOI: <https://doi.org/10.7554/eLife.28606.015>

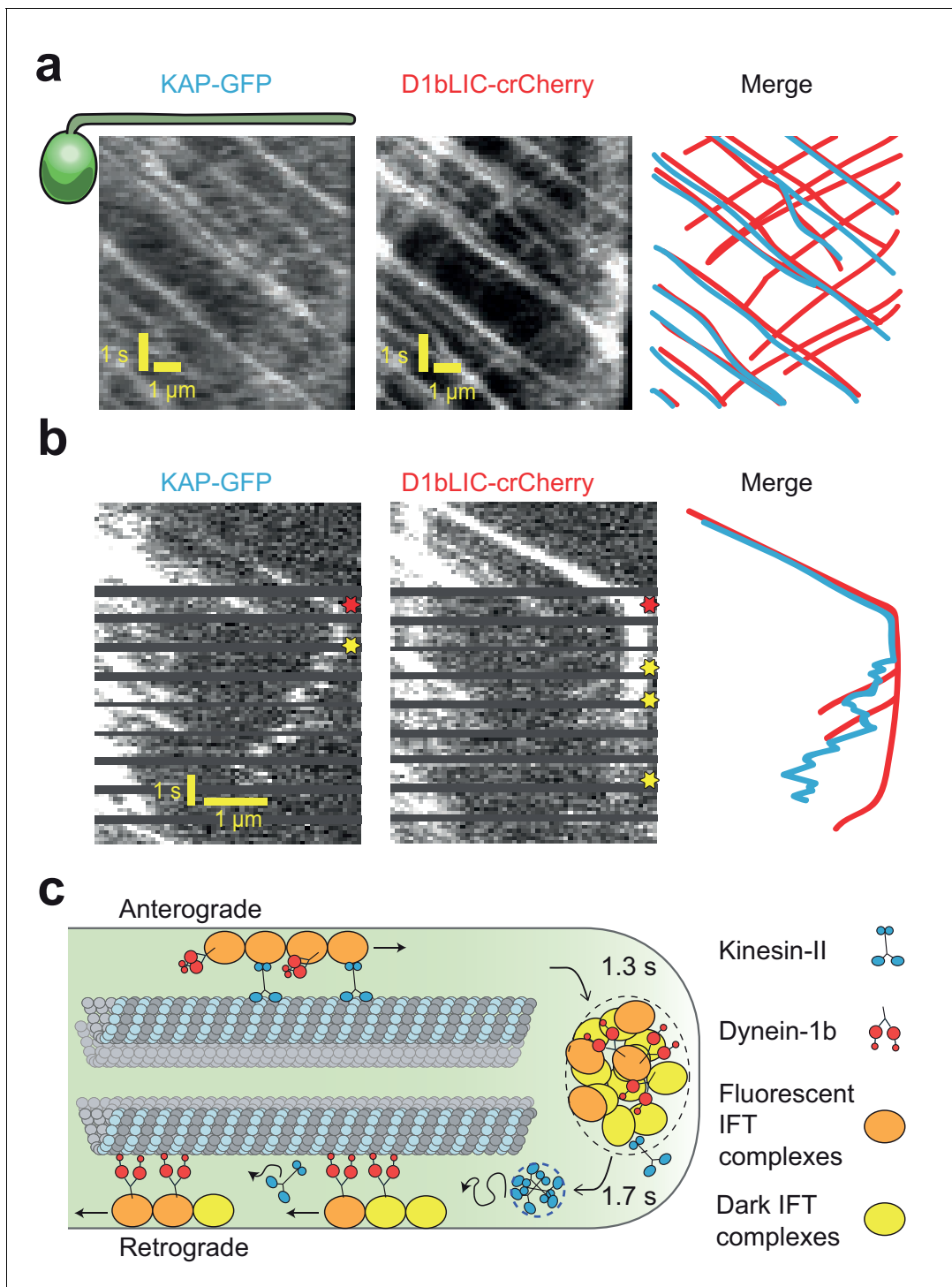


Figure 4. Transport roles of kinesin-II and dynein-1b. (a) Representative kymographs of KAP-GFP and D1bLIC-crCherry in a *d1blic::D1bLIC-crCherry* KAP-GFP flagellum. KAP-GFP and D1bLIC-crCherry co-localize on the IFT trains in the anterograde direction. Retrograde tracks are seen in the D1bLIC-crCherry channel, but are rarely visible in the KAP-GFP channel. (b) Example two-color PhotoGate trace of KAP-GFP (left) and D1bLIC-crCherry (middle) in single flagella. KAP-GFP and D1bLIC-crCherry arrive at the tip on the same train. In this example, KAP diffuses away from the tip before the departure of D1bLIC trains (right). Red and yellow stars indicate arrival to and departure from the flagellar tip, respectively. (c) A model for the turnover of IFT trains and motors at the flagellar tip. Kinesin-II motors transport individual anterograde IFT trains to the flagellar tip. Dynein-1b is carried with anterograde trains as an inactive passenger. At the tip, IFT complexes detach from microtubules, disassemble, and mix with the tip protein pool to assemble new trains. These trains are transported retrogradely by dynein-1b. Kinesin-II detaches from IFT trains at the flagellar tip and diffuses back to the base by diffusion either as a cluster (blue dashed circle) or individually.

DOI: <https://doi.org/10.7554/eLife.28606.019>

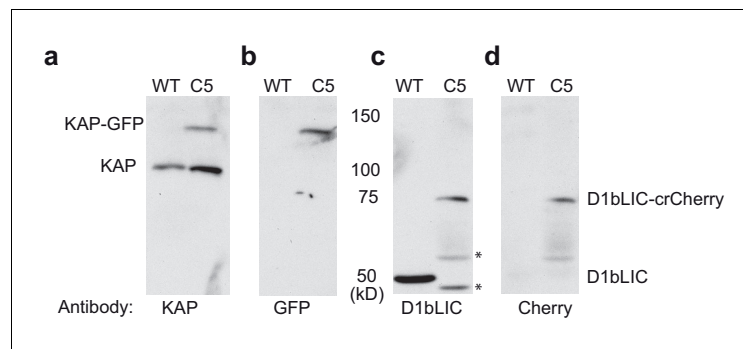


Figure 4—figure supplement 1. Expression of KAP-GFP and D1bLIC-crCherry in isolated flagella from a double-tagged strain. Isolated flagella from wild-type cells (WT) and a *d1blic::D1bLIC-crCherry KAP-GFP* strain (C5) were analyzed on Western blots probed with antibodies against (a) KAP, (b) GFP, (c) D1bLIC, and (d) Cherry. The endogenous KAP subunit migrates at ~95 kD in both strains (a), and the KAP-GFP subunit migrates at ~122 kD (a, b). The D1bLIC subunit migrates at ~49 kD in WT (c) and the D1bLIC-crCherry migrates at ~75 kD in the C5 rescued strain (c, d). The lower molecular weight bands in the C5 rescued strain represent proteolytic fragments of the D1bLIC-crCherry polypeptide (black asterisks). These bands are variable in preparations of isolated flagella.

DOI: <https://doi.org/10.7554/eLife.28606.020>

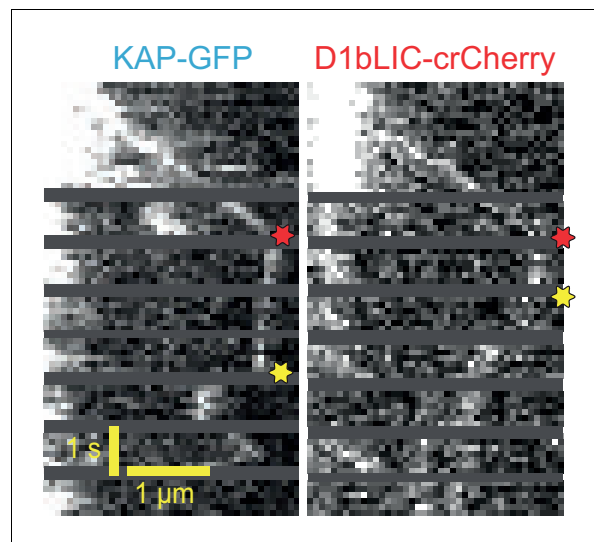


Figure 4—figure supplement 2. Example two-color PhotoGate trace of KAP-GFP (left) and D1bLIC-crCherry (right) in single flagella. KAP-GFP and D1bLIC-crCherry arrive at the tip on the same train. In this example, D1bLIC leaves the tip before KAP. Red and yellow stars indicate arrival to and departure from the flagellar tip, respectively.

DOI: <https://doi.org/10.7554/eLife.28606.021>

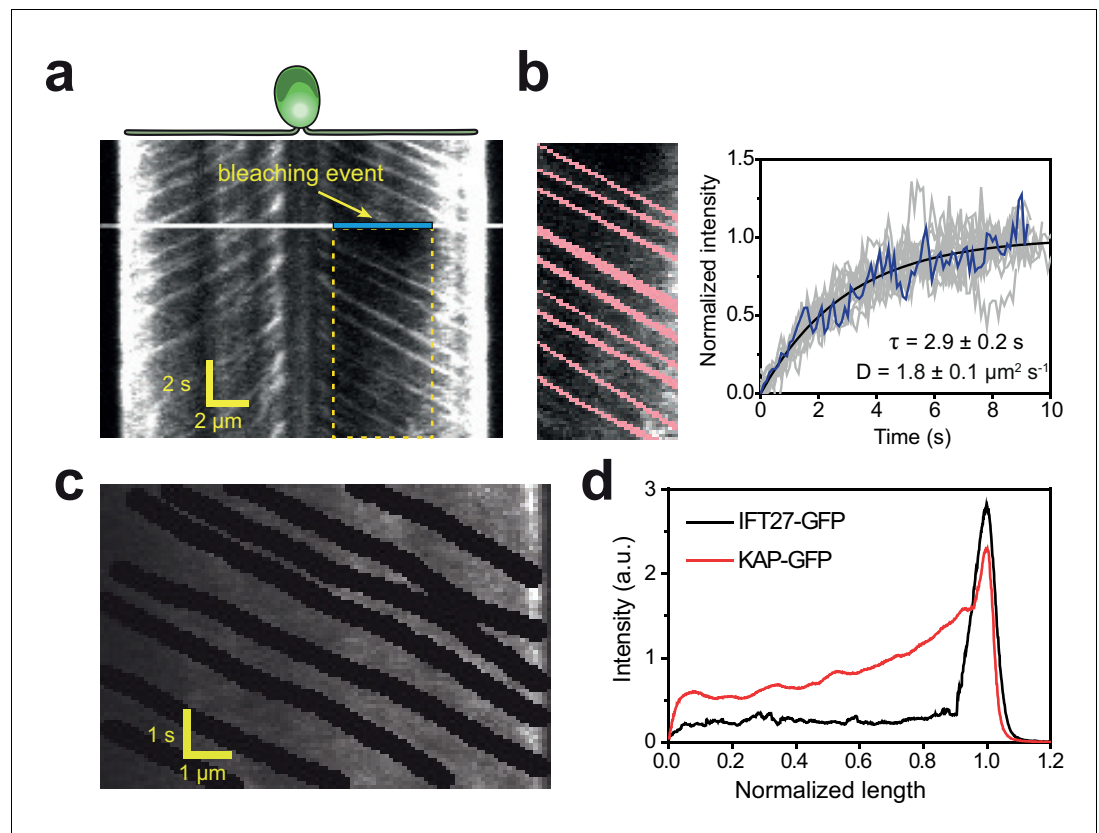


Figure 5. Diffusion of KAP from the flagellar tip leads to a concentration gradient along the flagellum. (a) Kymograph of KAP-GFP movement before and after photobleaching the middle section of the flagellum (blue area). While fluorescence recovery from the base is through anterograde movement, the recovery from the tip region is due to diffusion. (b) (Left) The GFP signal of anterograde traces (red) was manually subtracted from the rectangular area shown in (a). (Right) The intensity in the photobleached area shows recovery as a function of time (blue line). The average recovery signal of 13 cells (grey lines) was fitted to a one-dimensional diffusion equation (black curve, $\pm 95\%$ c.i.). (c) In conventional TIR imaging, anterograde trajectories of KAP-GFP were manually subtracted from the kymograph. (d) The average GFP signal along the length of a flagellum in KAP-GFP and IFT27-GFP cells after the removal of anterograde and retrograde transport traces from the kymographs. Flagellar base and tip positions were normalized to 0 and 1, respectively. $N = 11$ for both KAP-GFP and IFT27-GFP. DOI: <https://doi.org/10.7554/eLife.28606.023>

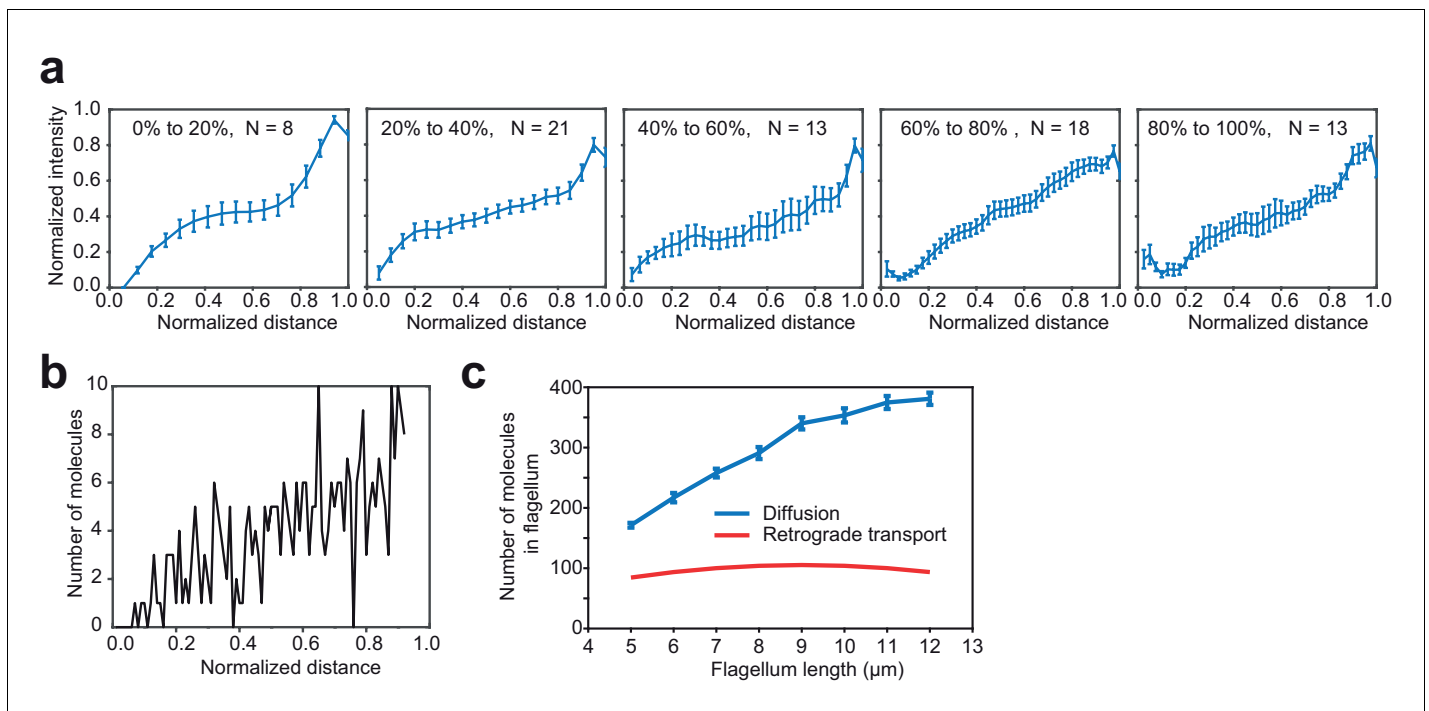


Figure 5—figure supplement 1. A gradient of KAP-GFP fluorescence along the length of the flagellum exists across all flagellar lengths. (a) The gradient of KAP-GFP fluorescence is approximately linear over the length of the flagellum for flagella of different lengths. Cells undergoing flagellar regrowth were imaged and split into groups by their flagellar length, as a percentage of full-length flagella. IFT trains were manually removed from kymographs and remaining pixels were time-averaged to calculate the concentration gradient of the KAP-GFP. Error bars represent s.e.m. $N = 57$ kymographs over five independent experiments. (b) Monte Carlo simulations reveal the flagellar distribution of KAP-GFP diffusing from a source at the tip (right) to a sink at the base (left). (c) Simulations show that return of KAP to the cell body by diffusion leads to a greater accumulation of KAP in the flagellum, in comparison to a hypothetical case where KAP returns to the cell body via retrograde transport. This analysis accounts for both anterogradely moving and diffusing KAP molecules.

DOI: <https://doi.org/10.7554/eLife.28606.024>

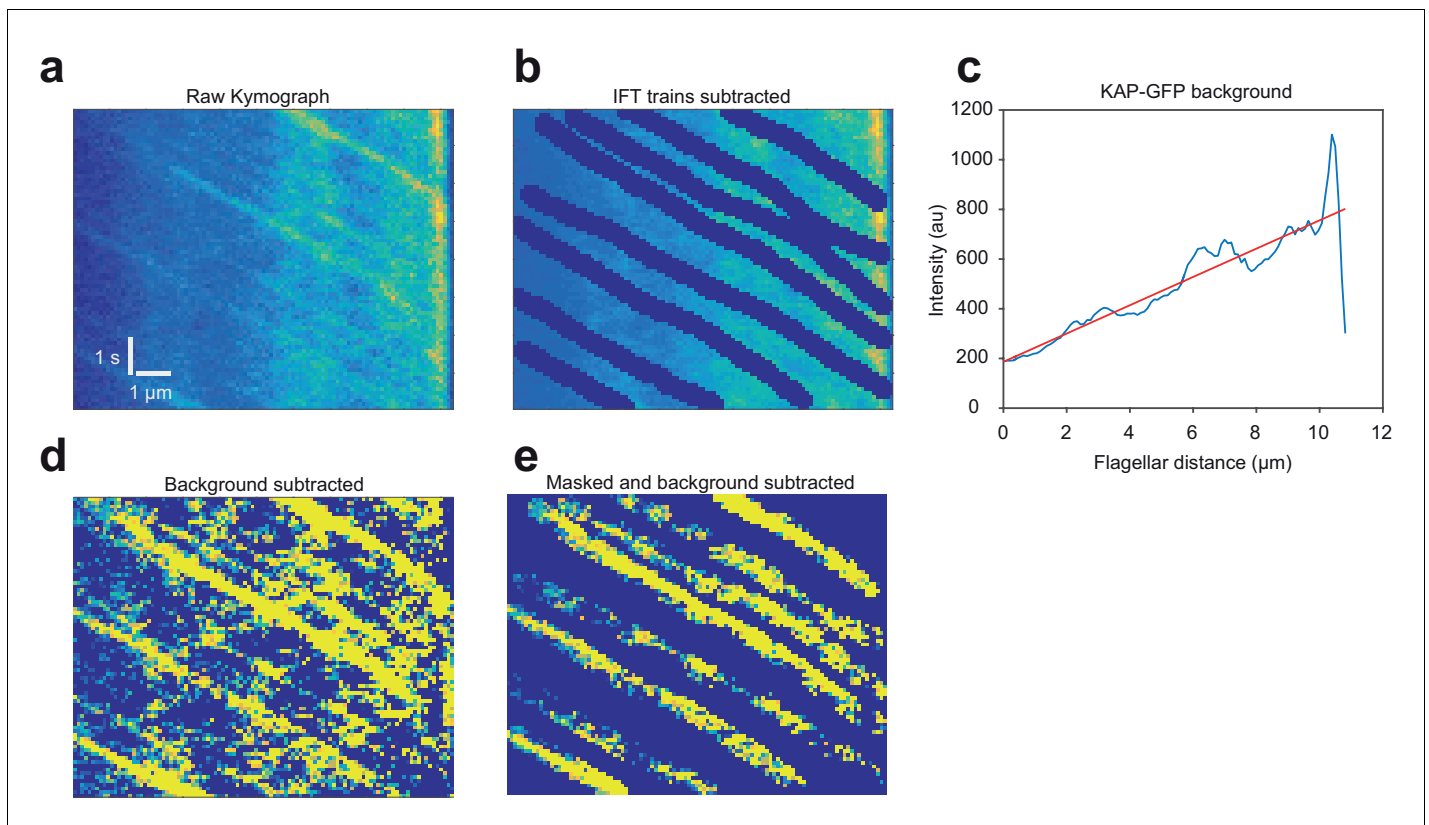


Figure 5—figure supplement 2. The influx and efflux of KAP-GFP fluorescence in fully grown flagella are equal. (a) An example kymograph of a *fla3::KAP-GFP* flagellum imaged with TIR. The flagellar tip is on the right. (b) To calculate the intensity of the fluorescence background, anterograde trajectories of KAP were manually subtracted from the kymograph. (c) Intensities were time-averaged to calculate KAP-GFP background. Efflux was calculated from Fick's law using the slope of the intensity profile along the flagellar length and the measured diffusion constant ($1.7 \mu\text{m}^2 \text{s}^{-1}$). (d) Background was subtracted from original kymograph to get anterograde train intensities. (e) The kymograph was masked for anterograde trains to calculate the average fluorescent counts per train. Influx was calculated by multiplying counts per train with the measured train frequency (1.3s^{-1}). KAP-GFP influx into the flagellum ($1,130 \pm 70 \text{ counts s}^{-1}$) was similar to the efflux of KAP from the flagellum ($1,170 \pm 160 \text{ counts s}^{-1}$). $N = 57$ kymographs over five independent experiments (mean \pm s.e.m.).

DOI: <https://doi.org/10.7554/eLife.28606.025>

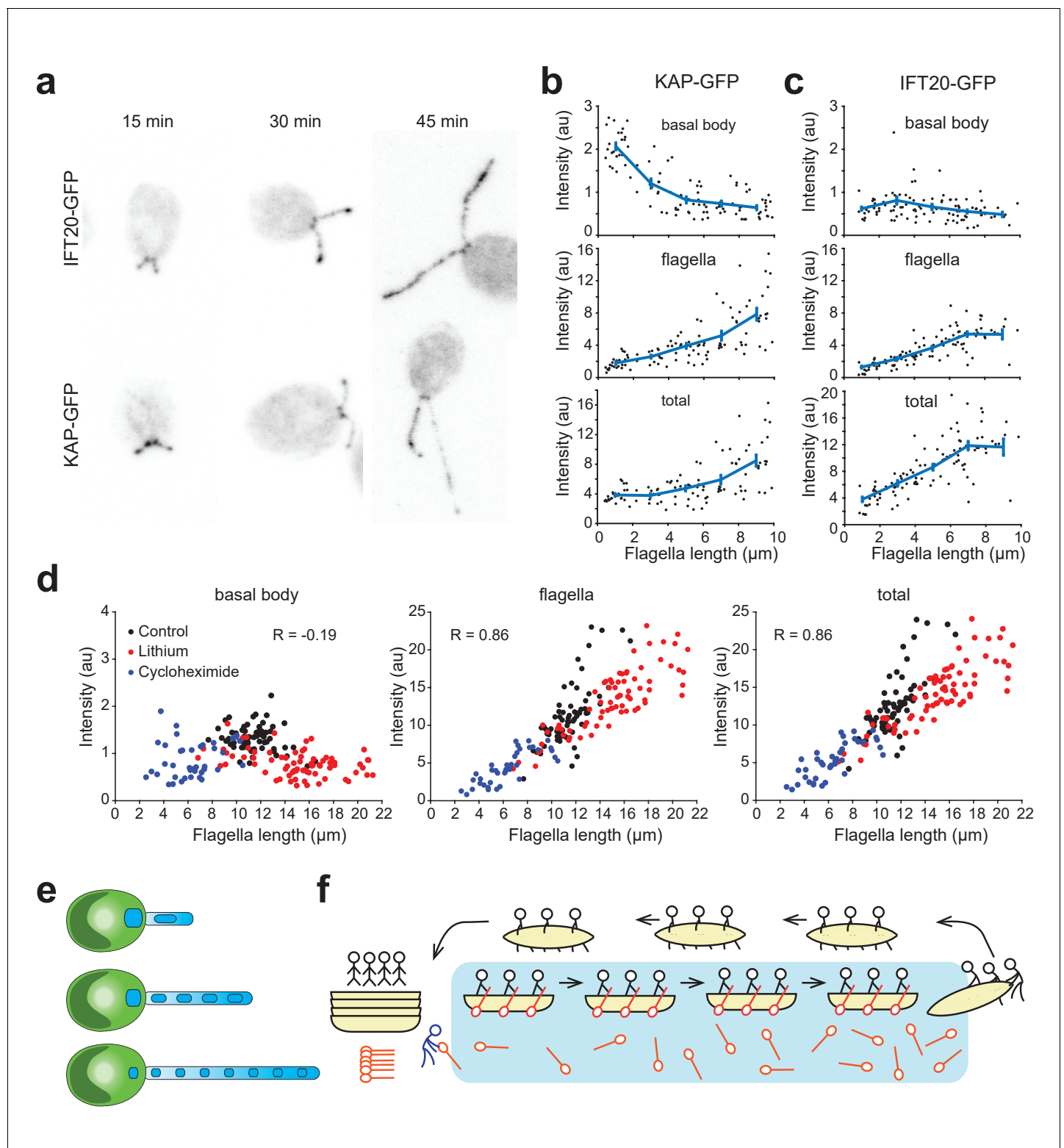


Figure 6. Kinesin-II accumulates in flagella and is depleted at the basal body during flagellar growth. (a) Representative confocal images show the distribution of IFT20-GFP and KAP-GFP fluorescence at the basal body region and in the flagella during flagellar regrowth. (b,c) Integrated KAP-GFP (b) and IFT20-GFP (c) fluorescence at the basal body (top), in the flagellum (middle), and in both regions (bottom) at different flagellar lengths. Each black dot represents a single flagellum and the blue line is the running average (\pm s.e.m.). For KAP-GFP, $N = 104$ flagella from 70 cells over two independent experiments. For IFT20-GFP, $N = 103$ flagella from 56 cells over two independent experiments. (d) Integrated KAP-GFP fluorescence at the basal body, flagella, and total flagella for Control, Lithium, and Cycloheximide treatments. *Figure 6 continued on next page*

Figure 6 continued

(left), in the flagellum (middle), and in both regions (right) in control cells was compared to cells treated with 50 mM Li^+ , and cells that regrow their flagella after cycloheximide treatment. R represents Pearson's correlation coefficient. Each dot represents a single flagellum. For control cells, $N = 66$ flagella from 33 cells. For lithium-treated cells, $N = 74$ flagella from 37 cells. For cycloheximide-treated cells, $N = 40$ flagella from 20 cells. (e) A model for flagellar length control. When the flagellum is short, IFT trains contain more kinesin-II from the large basal body pool. As flagella elongate, the number of kinesin-II per IFT train decreases because a significant fraction of the kinesin-II unloads at the tip and undergoes diffusion in the flagellar lumen, depleting the kinesin-II pool at the flagellar base. (f) An analogy for kinesin-II loading on IFT trains. Passengers (dynein-1b) travel from the left shore (basal body) to the right shore (flagellar tip) on a boat (IFT trains) with oars (kinesin-II). At the right shore, the passengers get out and walk the boats back to the dock. Oars are left on the water and can only be collected when they randomly float back to the left shore. If the distance between the shores is large, oars build up on the water and are not readily available for new boats at the left shore.

DOI: <https://doi.org/10.7554/eLife.28606.027>

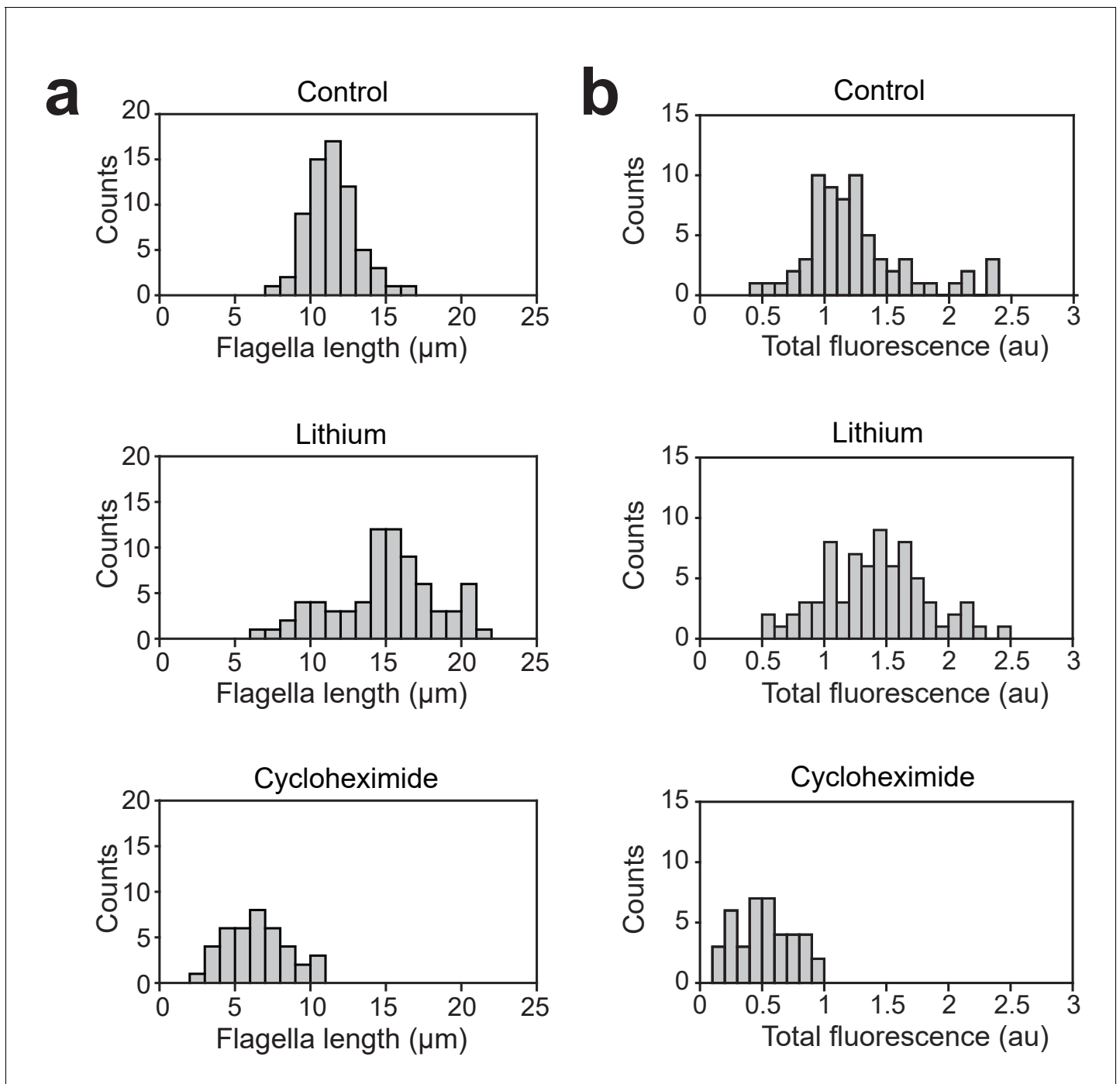


Figure 6—figure supplement 1. Length and total fluorescence distributions of lithium and cycloheximide-treated cells. (a) Flagella length distributions for *fla3::KAP-GFP* cells cultured in TAP media, cells treated with 50 mM LiCl, and cells subjected to pH shock and allowed to regrow flagella in the presence of 1.5 $\mu\text{g/ml}$ cycloheximide. For control cells, $N = 66$ flagella from 33 cells. For lithium-treated cells, $N = 74$ flagella from 37 cells. For cycloheximide-treated cells, $N = 40$ flagella from 20 cells. (b) Histograms show the total fluorescent signal of KAP-GFP localized to the basal body and the flagellum of single cells.

DOI: <https://doi.org/10.7554/eLife.28606.028>